Article

Not peer-reviewed version

Single-Cell Profiling Reveals Immune-Based Mechanisms Underlying the Tumor Radiosensitization by a Novel Mn Porphyrin Clinical Candidate, MnTnBuOE-2-PyP^{5+} (BMX-001)

Sun Up Noh , Jinyeong Lim , Sung-Won Shin , Yeeun Kim , Woong-Yang Park , Ines Batinic-Haberle , Changhoon Choi * , Won Park *

Posted Date: 6 February 2024

doi: 10.20944/preprints202402.0355.v1

Keywords: Mn porphyrin clinical candidate, MnTnBuOE-2-PyP^{5+} (BMX-001, MnBuOE); Single-cell RNA sequencing; Tumor heterogeneity; Tumor microenvironment; Radiotherapy; Tumor radiosensitization

Article

Single-Cell Profiling Reveals Immune-Based Mechanisms Underlying the Tumor Radiosensitization by a Novel Mn Porphyrin Clinical Candidate, MnTnBuOE-2-PyP^{5+} (BMX-001)

Sun Up Noh [1,2,†], Jinyeong Lim [3,4,†], Sung-Won Shin [1], Yeeun Kim [1], Woong-Yang Park [3,4], Ines Batinic-Haberle [5], Changhoon Choi [1,*] and Won Park [1,2,*]

1 Department of Radiation Oncology, Samsung Medical Center, Seoul 06351, Republic of Korea; chocolatebox919@gmail.com (S.U.N.); camuserik@gmail.com (S.-W.S.); yeeun17.kim@sbri.co.kr (Y.K.); chchoi93@gmail.com (C.C.); wonro.park@samsung.com (W.P.)
2 Sungkyunkwan University School of Medicine, Seoul 06351, Republic of Korea
3 Department of Health Sciences and Technology, Samsung Advanced Institute for Health Sciences and Technology, Sungkyunkwan University, Seoul 06351, Republic of Korea; aster1217@gmail.com (J.L.); woongyang.park@samsung.com (W.-Y.P.)
4 Samsung Genome Institute, Samsung Medical Center, Sungkyunkwan University, Seoul 06351, Republic of Korea
5 Department of Radiation Oncology, Duke University School of Medicine, Durham, NC 27710, USA; ibatibic@duke.edu (I.B.-H.)
* Correspondence: wonro.park@samsung.com (W.P.); chchoi93@gmail.com (C.C.) ; Tel.: +82-2-3410-2600 (W.P.)
† These authors contributed equally to this work.

Abstract: Manganese porphyrins reportedly exhibit synergic effects when combined with irradiation. However, an in-depth understanding of intratumoral heterogeneity and immune pathways, as affected by Mn porphyrins, remains limited. Here, we explored the mechanisms underlying immunomodulation of a clinical candidate, MnTnBuOE-2-PyP^{5+} (BMX-001, MnBuOE), using single-cell analysis in murine carcinoma model. Mice bearing 4T1 tumors were divided into 4 groups: control, MnBuOE, radiotherapy (RT), combined MnBuOE and radiotherapy (MnBuOE/RT). In epithelial cells, epithelial-mesenchymal transition, TNF-α signaling via NF-κB, angiogenesis, and hypoxia-related genes were significantly downregulated in the MnBuOE/RT compared to the RT. All subtypes of cancer-associated fibroblasts (CAFs) were clearly reduced in MnBuOE and MnBuOE/RT. Inhibitory receptor-ligand interactions, in which epithelial cells and CAFs interacted with CD8+ T cells, were significantly lower in the MnBuOE/RT than in the RT. Trajectory analysis showed that DC maturation-associated markers were increased in MnBuOE/RT. M1 macrophages were significantly increased in the MnBuOE/RT compared to the RT, whereas myeloid-derived suppressor cells were decreased. CellChat analysis showed that the number of cell-cell communications was the lowest in the MnBuOE/RT. Our study is the first to provide evidence for the combined radiotherapy with a novel Mn porphyrin clinical candidate, BMX-001 from the perspective of each cell-type within the tumor microenvironment.

Keywords: Mn porphyrin clinical candidate, MnTnBuOE-2-PyP^{5+} (BMX-001, MnBuOE); Single-cell RNA sequencing; Tumor heterogeneity; Tumor microenvironment; Radiotherapy; Tumor radiosensitization

1. Introduction

Currently, several anticancer treatment options are available, such as chemotherapy, immunotherapy, hormone therapy, surgery, and radiation. Among those, radiation therapy (RT) may be particularly effective for treating localized or solid cancers. Approximately half of all patients with cancer receive RT as a curative or palliative treatment. Moreover, as an adjuvant, RT is frequently combined with other types of treatment such as chemotherapy and surgery. However, the side effects

 doi:10.20944/preprints202402.0355.v1

of RT, which originate from reactive species-driven oxidative stress injury of normal tissue, have further prompted the development of safer and targeted therapies [1–4]. Radiation paradoxically triggers various changes in the tumor microenvironment (TME) that may lead to the risks of relapse and metastasis.

The differential impact of cationic manganese-substituted pyridylporphyrins on both normal and tumor tissues has been extensively [5,6]. These compounds sensitize tumors to radio- and chemotreatment and simultaneously protect normal tissue via modulation of their redox status [7]. The effect of Mn porphyrins, commonly known as superoxide dismutase (SOD) mimic, has been studied in various tumors, such as breast, head and neck, prostate, and brain [8–11]. The promising data obtained from cellular and animal studies have facilitated the progress of Mn(III) *meso*-tetrakis (*N*-n-butoxyethypyridinium-2-yl) porphyrin, i.e., MnTnBuOE-2-PyP^{5+} (BMX-001, MnBuOE) into clinic trials. With good safety/toxicity profile MnBuOE is presently tested on normal tissue protection, while tumor growth suppression in four Phase II clinical trials on patients bearing glioma, head and neck cancer, anal cancer and multiple brain metastases [5,12–15]. In addition, a recent glioblastoma study has shown that patients with glioblastoma have improved survival rates when combination treatment of Mn porphyrin clinical candidate, MnBuOE (BMX-001) with irradiation [16]. The biocompatible redox properties of Mn porphyrins, their ability to interact with numerous reactive species, their bioavailability within cells and cellular compartments, and the tumor heterogeneity of immunogenic and metabolic pathways necessitate additional studies on the nature of the differential actions of Mn porphyrins within the TME. Previously, we explored the anticancer potency and metabolic pathways affected by an earlier analog, MnTnHex-2-PyP^{5+} [17,18]. Here, considering the progress of Mn porphyrins into clinical settings, we have further explored the complex metabolic pathways that play important roles in the anticancer activities of the clinical candidate, MnBuOE (BMX-001).

Despite the evidence supporting the role of Mn porphyrins in cancer therapy, little is known about their immunomodulatory effects. Thus far, studies on these compounds have been limited to total RNA-sequencing [19]. In a previous study, we assumed that Mn porphyrins could inhibit RT-induced epithelial-to-mesenchymal transition (EMT) in the TME by suppressing pro-survival signaling pathways, the AKT/GSK3β/Snail pathway, and NF-kB activation in a mouse 4T1 tumor in vitro or in vivo [18]. However, our understanding of the molecular mechanisms of Mn porphyrins has been largely limited to the estimation of the average gene expression of tumor cells.

Tumors are intricate ecosystems. The TME is composed of diverse cells, including cancer cells and stromal subsets, whose specific characterization is masked by heterogeneity. Numerous studies have suggested that stromal cells, such as epithelial cells, T cells, macrophages, and fibroblasts, which are highly heterogeneous, are associated with tumors [20–24]. Tumor heterogeneity governs many decisive facets of tumor pathogenesis that are driven by tumor growth, metastasis, and resistance to treatment. Therefore, it is essential to examine the gene expression patterns of individual cells.

Single-cell RNA sequencing (scRNA-seq) enables specific profiling of individual cell populations, thereby enabling unbiased distinguishing of heterogeneous stromal and cancer cells at the resolution of individual cells. Therefore, scRNA-seq techniques have emerged as promising methods for elucidating tumor pathogenesis, revealing the complexities of and differences between the molecular components [25,26]. Furthermore, understanding the correlation between cancer and stromal/immune cells in the TME and identifying potential targets could be particularly important for determining the synergistic effect of MnBuOE/RT. In this study, we aimed to explore how Mn porphyrin clinical candidate, MnBuOE (BMX-001) and RT affect the characteristics of tumor and stromal cells in murine mammary carcinoma using scRNA-seq.

2. Materials and Methods

2.1. Animal Models

For the establishment of the 4T1 tumor model, 6–7-week-old female BALB/c mice were purchased from Orient Bio (Gapyeong, Korea) and cells (1 x 10^5 cells in 50 μL phosphate-buffered

 doi:10.20944/preprints202402.0355.v1

saline) were injected subcutaneously into the right hind leg of each mouse. Tumor volumes were measured every 3 days using calipers and calculated as volume = (width^2 × length)/2. When the mean tumor volume reached 80–120 mm^3, the mice were randomly divided into four groups: control group (CN), MnTnBuOE-2-PyP^{5+} group (MnBuOE), radiotherapy group (RT), and group receiving MnBuOE along with radiotherapy (MnBuOE/RT). MnBuOE was injected intraperitoneally (1 mg/kg) twice a week. Two hours after drug administration, irradiation was conducted on the tumor-bearing hind leg over 3 continuous days at 2 Gy X-ray for a total of 6 Gy. During irradiation, the mice were anesthetized via intraperitoneal injection of 30 mg/kg Zoletil (Virbac, Carros, France) and 10 mg/kg Rompun (Bayer, Leverkusen, Germany), as prescribed by veterinarians. Fifteen days after irradiation, all tumor tissues were isolated and excised. Some tumor tissues were prepared for scRNA-seq and flow cytometric assay. Other tumor tissues were fixed with 10% formalin and embedded in paraffin for terminal deoxynucleotidyl transferase(TdT)-mediated biotinylated dUTP nick end labeling (TUNEL) analysis. The study protocol (20220210001) was reviewed and approved by the Institutional Animal Care and Use Committee (IACUC) of the Samsung Medical Center (SMC). SMC is an Association for Assessment and Accreditation of Laboratory Animal Care International accredited facility and abides by the Institute of Laboratory Animal Resources guidelines.

2.2. Tissue Dissociation Into Single-Cell Suspension

Tumor tissues were dissected from the mice and dissociated into single-cell suspensions via mechanical dissociation combined with enzymatic degradation of the extracellular matrix (ECM), which maintains the structural integrity of tissues. The tumor tissue was enzymatically digested using Tumor Dissociation Kit (Miltenyi Biotec., Bergisch Gladbach, Germany), and gentleMACS™ Dissociators (Miltenyi Biotec.) were used for mechanical dissociation. After dissociation, a filter was used to remove any remaining larger particles from the single-cell suspension.

2.3. Single-Cell RNA Sequencing Data Processing

The single-cell suspensions were washed and loaded onto a Chromium single cell system (10x Genomics, Pleasanton, CA, USA). The barcoded sequencing libraries were created using the Chromium Single Cell 5′ Reagent kits (10x Genomics) according to the manufacturer's instructions and then sequenced on a Novaseq6000 platform (Illumina, San Diego, CA, USA). The resulting sequencing data were aligned to the mouse reference genome (GRCm38) and processed through the CellRanger 4.0.0 pipeline (10x Genomics). A stringent selection process was imposed to exclude cells that failed to reach sufficient cell quality threshold. Specifically, cells exhibiting fewer than 500 unique molecular identifier (UMI) counts, fewer than 250 detected genes, more than 30% mitochondrial gene expression, or low cell complexity (l log10GenesPerUMI l ≤ 0.8) were omitted. Ensuring the singularity of cell population and the exclusion of potential doublets, the "DoubletFinder" package (Version 2.0.3) was employed. Consequently, approximately 10 % of cells were annotated low quality of cells (4,231 of 39,585) and excluded from the subsequent analysis. Single-cell analysis was performed in Seurat R package. Specifically, the gene expression matrices were normalized and transformed to the log scale. For feature selection, the top 2,000 highly variable genes expressed in each sample were chosen.

2.4. Cluster Identification and Annotation

For clustering, the variably expressed genes were subjected to a principal component analysis (PCA). The number of principal components selected for the major cluster or subset clusters was determined by evaluating the slope of the elbow plot. Both PCA and uniform manifold approximation and projection (UMAP) dimension reduction were performed using the selected PCs. The nearest-neighbor graphs were calculated using the same PC dimensions from the PCA reduction, and clustering was performed. To determine the cell type for the major cluster or subset clusters, differentially expressed genes (DEGs) were determined using the "findmarker" function in Seurat R packages based on the Model-based Analysis of Single Cell Transcriptomics test with a minimal

 doi:10.20944/preprints202402.0355.v1

fraction of 25% and a log-transformed fold change threshold of 0.25 [27,28]. Additionally, canonical markers for scRNA-seq data from relevant literature were used. To visualize the canonical markers and DEGs, heatmaps, dot plots, and violin plots were generated to show the expression of the markers used for identifying each cell type.

2.5. Pathway Enrichment Analysis

To identify biological functions or pathways that were significantly associated with specific cell types or gene sets, we performed a gene set variation analysis (GSVA) with the hallmark gene sets from the Molecular Signatures Database (Msigdb) using the average gene expression of each cell type or group. Additionally, we conducted a gene set enrichment analysis (GSEA) by ranking the DEGs of each targeted cluster or group according to log-transformed fold change (logFC) and then utilizing this ranked list as input for the fgsea function in the fgsea R package [29].

2.6. Trajectory Analysis

Cell lineage analysis in dendritic cells (DCs) was performed using the monocle v.2 package [30]. We reconstructed the single-cell trajectory by creating a monocle object using the UMI count metrics and the "negbinomial.isze" parameter with default settings. To identify DEGs, we used the differentialGeneTest function to select the top 300 genes with the lowest q-values. Dimensional reduction and cell ordering were conducted using the DDRTree method and the orderCells function, respectively.

2.7. Cell–Cell Communication and Receptor–Ligand Interaction Analysis

The cell–cell interactions based on the expression of ligand-receptor pairs in different cell types were inferred using the CellChat R package [31]. We followed the recommended workflow in CellChat and utilized the default settings to identify major signaling interactions and evaluate the coordination of cells and signals for various functions. Briefly, the normalized counts were used as a CellChat object and subjected to the preprocessing functions, including identifyOverExpressedGenes, identifyOverExpressedInteractions, and projectData with the default parameters. The strength of ligand-receptor interactions and the number of interactions were determined using the computeCommunProb, compute-CommunProbPathway, and aggregateNet functions with the default parameters applied in a stepwise manner.

2.8. TUNEL Staining

Deparaffinized and dehydrated tumor tissue sections were stained by TUNEL In Situ Cell Death Detection Kit (Roche Applied Science, Mannheim, Germany) according to the manufacturer's protocol. Briefly, tumor tissue sections were placed in a 3% hydrogen peroxide solution with methanol to block endogenous peroxidase activity and were incubated in 0.1% sodium citrate containing 0.1% Triton X-100 to increase tissue permeability. After rinsing in PBS, 50 µl of TUNEL reaction mixture (calf thymus TdT and nucleotides) was added to each sample. After incubation at 37°C in the dark for 60 min, these sections were rinsed with PBS and the apoptotic cells were marked by 3,3′-diaminobenzidine (DAB) through horseradish peroxidase (HRP) catalysis of biotinylated dUTP-streptavidin-HRP. Images were captured using an Aperio ScanScope AT slide scanner (Leica Biosystems, Inc., Buffalo Grove, IL). Numbers of TUNEL-positive cells were determined with ImageScope software (Leica Biosystems, Inc.).

2.9. Flow Cytometric Analysis

Harvested tumors were cut into small pieces and dissociated using a Tumor Dissociation Kit according to the manufacturer's instructions (Miltenyi Biotec, Auburn, CA, USA). Red blood cells were lysed with BD Pharm Lyse™ lysing buffer (BD Bioscience, San Jose, CA, USA). Cell suspensions were stained with PerCP-Cy5.5-conjugated anti-CD45 antibody, FITC-conjugated anti-mouse CD3 antibody, APC-Cy7-conjugated rat anti-mouse CD4 antibody, V450-conjugated rat anti-mouse CD8

 doi:10.20944/preprints202402.0355.v1

antibody, APC-conjugated anti-mouse CD25 antibody, APC-Cy7-conjugated rat anti-mouse CD45 antibody, PerCP-Cy5.5-conjugated rat anti-mouse CD11b antibody, Alexa Fluor 647-conjugated rat anti-mouse F4/80 antibody, FITC-conjugated anti-CD86 antibody (BD bioscience), or PE-Cy7-conjugated anti-CD206 antibody (eBioscience, San Diego, CA, USA). For intracellular staining, cells were fixed and permeabilized with Fixation/Permeabilization buffer (eBioscience) and stained with PE-conjugated rat anti-mouse Foxp3 antibody (BD bioscience). Flow cytometric analysis was performed using a BD FACS Verse flow cytometer (BD bioscience) and FlowJo software version 10.6.1 (BD bioscience).

2.10. Statistical Analysis

GraphPad Prism 9.4.1 (GraphPad Software, San Diego, CA, USA) was used for all statistical analyses. Differences among groups were determined by Student's t-test with Bonferroni correction for comparison between two groups or one-way analysis of variance (ANOVA) following Tukey post hoc test. Tumor growth curves were analyzed using a two-way analysis of variance (ANOVA) with Tukey's correction for multiple comparisons. Statistical significance is presented as $*P<0.05$, $**P<0.01$, $***P<0.001$, or $****P<0.0001$. The statistical details of each experiment are indicated in the figure legends.

3. Results

3.1. Effect of MnBuOE Coupled with Irradiation and Major Single-Cell Mapping in the 4T1 Tumor Mouse Model

Inflated tumor volumes around the right hind leg were measured to evaluate the tumor growth trend for the experimental groups (CN, MnBuOE, RT, MnBuOE/RT) after induction of 4T1 tumors (Figure 1A-B). Tumor growth rapidly increased in the CN group after 9 days of tumor randomization (zero-day). Compared to the CN group, no significant change in tumor growth was observed in the MnBuOE group. However, significant reduction in tumor growth compared to the CN and MnBuOE groups ($P<0.05$) was observed in the MnBuOE/RT group. At 15 days, the tumor volume of the MnBuOE/RT group was reduced by approximately 61.2% compared with that of the MnBuOE group.

 doi:10.20944/preprints202402.0355.v1

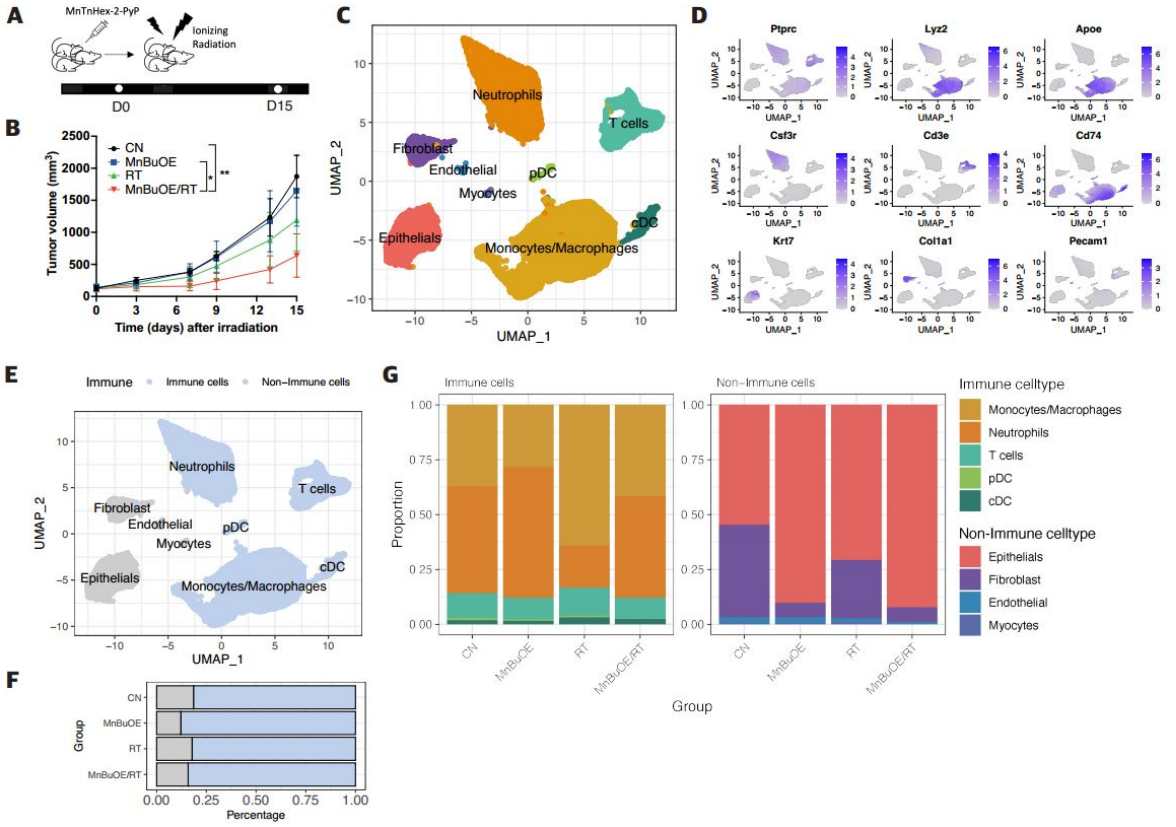

Figure 1. Effect of MnBuOE coupled with irradiation on major single-cell clustering in the 4T1 tumor mice model. (A,B) Tumor-bearing tissues were prepared for scRNA-seq 15 days after MnBuOE treatment and irradiation. The tumor volumes were measured once every 3 days. MnBuOE combined with radiation therapy increased tumor growth delay compared to MnBuOE monotherapy. **P*<0.05, ***P*<0.01. **(C)** After PCA and UMAP analysis of the UMI counts in all 35,354 single cells sorted from each group, the hierarchical clustering distinguished 8 major clusters: macrophages, neutrophils, T cells, DCs, epithelial cells, fibroblasts, endothelial cells, myocytes. **(D)** According to the expression of specific marker genes for various cell types, immune cell types (Ptprc), macrophages (Lyz2, Apoe), neutrophils (Csf3r), T cells (Cd3e), DCs (Cd74), epithelial cells (Krt7), fibroblasts (Col1a1), and endothelial cells (Pecam1) were identified. **(E-G)** The eight main cell subtypes were divided into immune cells and non-immune cells. Blue dots represent immune cells (macrophages, neutrophils, T cells, and DCs), whereas grey dots represent non-immune cells (epithelial cells, fibroblasts, endothelial cells, and myocytes). MnBuOE treatment increased the proportion of immune cells compared to the CN group. scRNA-seq, single-cell RNA sequencing; MnBuOE, MnTnBuOE-2-PyP^{5+}; PCA, principal component analysis; UMAP, uniform manifold approximation and projection; UMI, unique molecular identifier; DCs, dendritic cells.

The scRNA-seq analysis was performed to investigate the heterogeneous transcriptomic responses of tumor, stromal cells, and immune cells within each experimental cohort. Following the application of stringent quality filters to eliminate low-quality cells, the resulting dataset displayed a mean of 2,227 transcripts per cell, with an average of 10,362 reads per cell (Supplementary Figure S1A-B). Following PCA and UMAP visualization, unbiased clustering of all 35,354 single cells sorted from each group revealed 8 major clusters: macrophages (14,177 cells, 40.6% of the total), neutrophils (11,089 cells, 31.8% of the total), T cells (3,013 cells, 8.6% of the total), and DCs (consist of pDC and cDC, 892 cells, 2.5% of the total), epithelial cells (4,098 cells, 11.7% of the total), fibroblasts (1,390 cells, 3.9% of the total), endothelial cells (135 cells, 0.4% of the total), myocytes (103 cells, 0.2% of the total) (Figure 1C). The annotation of each cluster was facilitated through broad cell marker genes including *Ptprc* (immune cell), *Lyz2, Apoe* (Macrophage), *Csf3r* (Neutrophils), *Cd3e* (T cell), *Cd74* (Macrophage and DCs), *Krt7* (Epithelial cell), *Col1a1* (Fibroblasts) and *Pecam1* (Endothelial cells) (Figure 1D and Supplementary Figure S1C-D). A distinct partitioning of these major cell categories was

 doi:10.20944/preprints202402.0355.v1

distinguished into 29,171 immune cells (depicted in blue, 83% of the total) and 5,726 non-immune cells (denoted in gray, 16% of the total) (Figure 1E). Of note, the non-immune cell population in CN was most pronounced, constituting 20% of the total cell proportion. In contrast, the MnBuOE/RT group displayed a proportion of non-immune cell clusters, accounting for 15.6% of the total cell (Fig 1F). This reduction in non-immune cell proportions within the treatment group could be attributed to a concurrent reduction in tumors. Notably, among the nonimmune cell types, increased epithelial cells and decreased fibroblast in the MnBuOE treatment group showed clear characteristics (Fig 1G). This intriguing observation showed further comprehensive investigation to elucidate the underlying mechanisms and implications of such a response.

3.2. Epithelial Cell Clustering and Subtype Analysis of the 4T1 Tumor Treated with MnBuOE Coupled with Irradiation

To reveal the potential functional subtypes of the overall epithelial cell populations, 4,098 epithelial cells were re-clustered and identified four epithelial related cell clusters. These were identified based on corresponding unique signature genes and assigned to known epithelial cell types (Figure 2A-B and Supplementary Figure S2A-B). The first cluster, Epi1_Epcam-, was characterized by high expression of the Twist1 and Zeb2 genes, which are predominantly associated with mesenchymal cell polarization. In contrast, the second cluster, Epi2_Epcam+, distinguished by specific expression of Epcam and Cdh1 genes, was dominant in epithelial cell polarization. The third cluster, Epi3_cycling, was associated with cell proliferation and was identified by high Mki67 expression. The remaining cells, which formed the fourth cluster, Epi4_Rps, were excluded from further analyses owing to their lower quality. As shown in Figure 2D, the distribution patterns of epithelial cell clusters were comparable among experimental groups. The percentage of Epcam- cells in the MnBuOE/RT group (15%) was lower than that in the RT (35%). Moreover, the Epcam+ fraction in the MnBuOE/RT group (31%) was higher than that in the RT group (20%). The mesenchymal cell marker genes *Twist1* and *Zeb2* were significantly reduced in the MnBuOE/RT group compared to the other groups, and the epithelial cell marker gene *Cdh1* was increased in the MnBuOE/RT group compared to the RT group ($P<0.0001$, Figure 2E). Additionally, the expression of the *Vegfa* gene associated with angiogenesis and the *Hif1a* gene associated with hypoxia were significantly lower in the MnBuOE/RT group than in the other groups ($P<0.001$). The *Tgfb1* gene related to the inhibition of T-cell activation was significantly downregulated in the MnBuOE/RT group compared to the RT group ($P<0.0001$).

 doi:10.20944/preprints202402.0355.v1

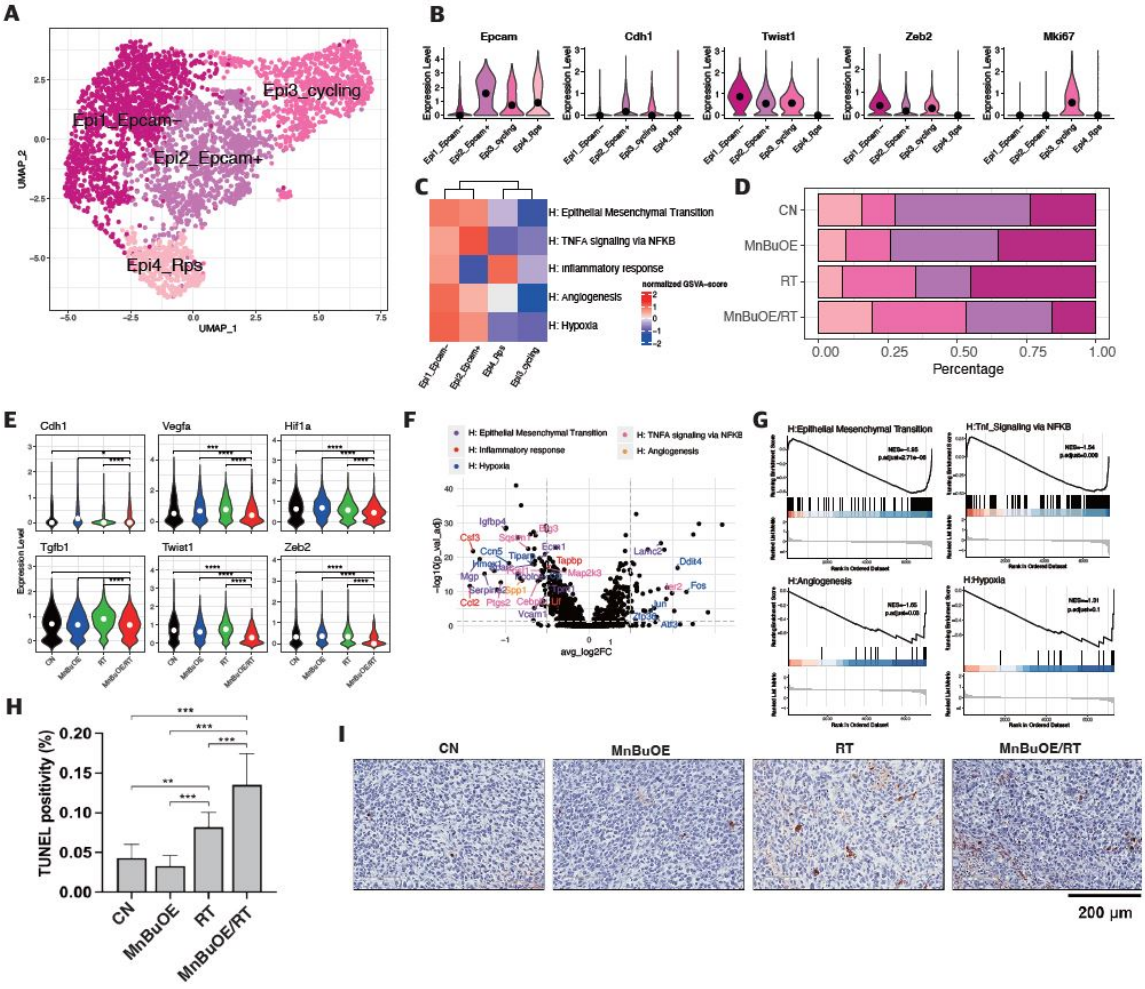

Figure 2. Effect of MnBuOE treatment and irradiation on cancer-associated pathways in epithelial cell subtypes of 4T1 tumor mice. (A) UMAP plot of epithelial cells indicated four subtypes: Epicam- (mesenchymal bias), Epicam+ (epithelial bias), cycling (proliferation), and Rps (non-function) types (n=4,098). (B) Violin plots show that expression of specific marker genes, including epithelial bias (Epcam, Cdh1), mesenchymal bias (Twist1, Zeb2), and cell proliferation (Mki67) differed between the different epithelial cell subtypes. (C) Heatmap of GSVA scores determined using Hallmark GeneSet (EMT, TNF-alpha signaling via NF-kB, inflammatory response, angiogenesis, and hypoxia) showed increased involvement in the Epicam- and Epicam+ subtypes for each experimental group. (D) All experimental groups included the fractions of four clusters of epithelial cell subtypes. (E) Violin plots indicated differential expression of *Cdh1, vegfa, Hif1, Tgfb1, Twist1, and Zeb2* between the different experimental groups. **P*<0.05, ****P*<0.001, *****P*<0.0001. (F) Volcano plot of DEGs in the MnBuOE/RT (MnBuOE and irradiation) versus RT (irradiation only) groups. The dot color represents the upregulated or downregulated DEGs, whereas the text color represents the related Hallmark pathway. (G) GSEA enrichment plots in relevant Hallmark gene sets in the MnBuOE/RT versus RT groups showing the NES score and adjusted p-values. The positions of gene set members on the rank-ordered list indicate the level of enrichment of the genes within the gene set. These results indicate that MnBuOE combined with radiation therapy markedly declined carcinogenesis pathways such as EMT, TNF-alpha signaling via NF-kB, inflammatory response, angiogenesis, and hypoxia compared to radiation therapy only. (H,I) TUNEL analysis and DAB staining showing increased apoptosis in tumor tissue sections of the MnBuOE/RT groups compared to the other groups. ***P*<0.01, ****P*<0.001. MnBuOE, MnTnBuOE-2-PyP^{5+}; UMAP, uniform manifold approximation and projection; GSVA, gene set variation analysis; EMT, epithelial-to-mesenchymal transition; DEGs, differentially expressed genes; MnBuOE/RT, MnTnBuOE-2-PyP^{5+}/radiation therapy; GSEA, gene set enrichment analysis; NES, normalized enrichment score; TUNEL, terminal deoxynucleotidyl transferase-mediated biotinylated dUTP nick end labeling; DAB, 3,3′-diaminobenzidine.

 doi:10.20944/preprints202402.0355.v1

GSVA was performed to determine the biological functions of each epithelial subtype in tumorigenicity and progression. The Epcam- and Epcam+ clusters had significantly enriched GSVA scores for pathways such as EMT, TNF-alpha signaling via NF-kB, inflammatory response, angiogenesis, and hypoxia (Figure 2C). In contrast, the cycling cluster showed high expression of genes involved in cell cycle pathways such as G2M checkpoint, E2F target, and DNA repair (data not shown). As shown in Figure 2F, we filtered a total of 90 DEGs using the criteria of |log2-fold change| ≥ 0.5 and $P<0.05$ between the MnBuOE/RT and RT groups. These DEGs were divided into two groups, containing 34 upregulated and 56 downregulated genes. We annotated these DEGs into hallmark gene pathways using Msigdb and color-coded the relevant pathways (EMT, TNF-alpha signaling via NF-kB, inflammatory response, angiogenesis, and hypoxia) in a volcano plot. Additionally, the DEGs were subjected to GSEA to investigate the key pathways and core genes between the RT and MnBuOE/RT groups. Figure 2G shows the GSEA enrichment plot of five hallmark pathways in the MnBuOE/RT group compared to the RT group, namely, EMT (Serpine2, Mgp, Vim, Vegfa and others), TNF-alpha signaling via NF-kB (Ccl2, Ptsg2, Cebpb, Areg, Btg3 and others), inflammatory response (Ifngr2, Axl, Selenos, Mmp14, Cd82, and others; data not shown), angiogenesis (App, Slco2a1, Vegfa, Spp1 and Lrpap1), and hypoxia (Ppp1r15a, Prdx5, Aldoc, Phha2, Ldha and others). We observed that the biological pathways relevant to EMT, TNF-alpha signaling via NF-kB, inflammatory responses, angiogenesis, and hypoxia were significantly downregulated in the MnBuOE/RT group compared with the RT group ($P<0.05$). In particular, apoptosis-related gene analysis using Msigdb did not show discrimination between experimental groups, but TUNEL staining showed significantly higher TUNEL-positive cells in the MnBuOE/RT group compared to the rest of the groups, indicating an increased apoptosis ($P<0.001$, Figure 2H-I).

3.3. Fibroblasts Clustering and Subtype Analysis of the 4T1 Tumor Treated with MnBuOE Coupled with Irradiation

The 1,390 fibroblasts were clustered in three separate subsets (Supplementary Figure S3A) corresponding to inflammatory, myofibroblastic, and cycling cancer-associated fibroblasts (CAFs). We observed distinct phenotypic differences that enabled the characterization of their functions in greater detail (Supplementary Figure S3B, S3E). For instance, chemokine markers involved in angiogenesis or inflammation such as Cxcl1, Cxcl2, and Cxcl12 were mainly upregulated in inflammatory CAFs, whereas myogenic markers such as Tagln, Acta2, and Mmp9 showed the highest expression in myofibroblastic CAFs. Expression of the cell proliferative marker Mki67 was increased in cycling CAFs. Remarkably, most of the CAFs, including myofibroblastic and inflammatory CAFs, substantially declined in the MnBuOE treatment groups (MnBuOE, MnBuOE/RT) compared to the CN and RT groups (Supplementary Figure S3C-D). We confirmed that the number of myofibroblastic CAFs decreased from 39 to 6 and that of inflammatory CAFs decreased from 143 to 7 in the MnBuOE/RT group compared to those in the RT group. These results showed that MnBuOE treatment resulted in CAF removal in the 4T1 tumor model.

Preprints.org (www.preprints.org) | NOT PEER-REVIEWED | Posted: 6 February 2024 doi:10.20944/preprints202402.0355.v1

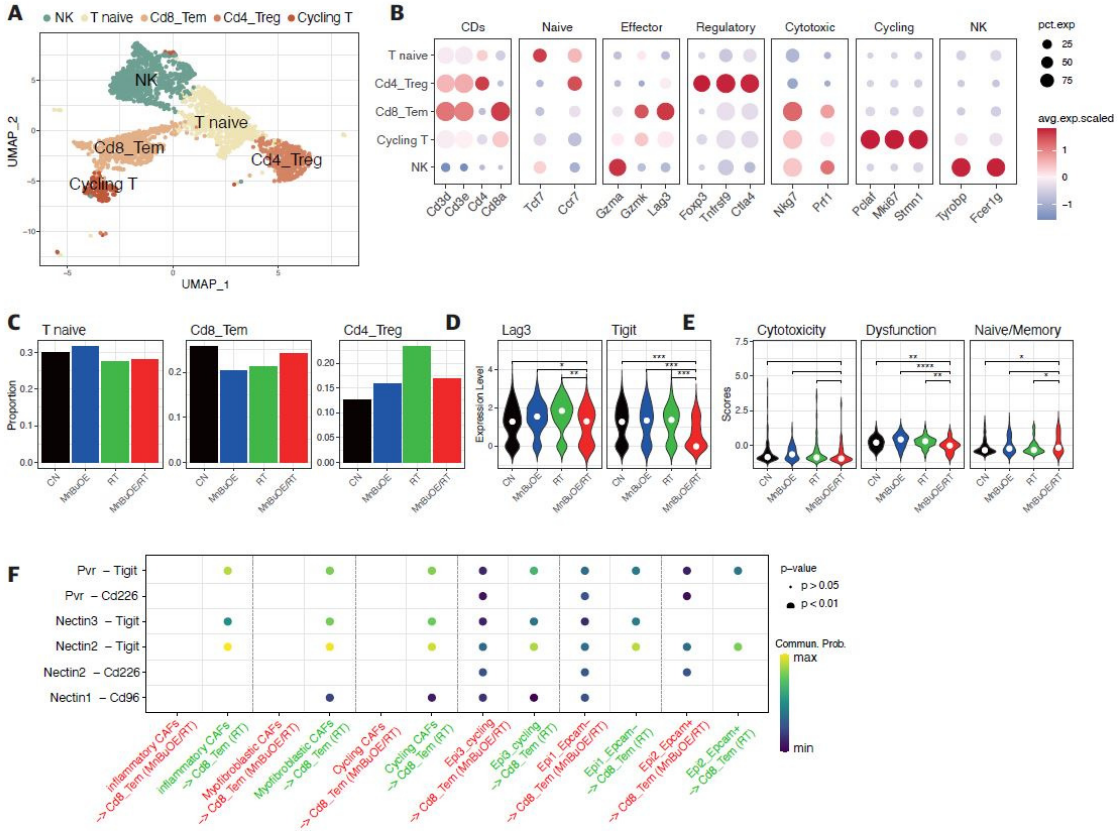

Figure 3. Decreased Tigit expression and cell–cell interaction in CD8 effector T cells following treatment with MnBuOE and irradiation. (A) UMAP plot of T cells indicated the formation of five main clusters shown in different colors (n=3,013). (B) Dot plot of canonical T cell markers in each subtype, i.e., NK (Gzma, Tyrobp, Fcer1g), T naïve (Tcf7, Ccr7), Cd8_Tem (Cd3d, Cd3e, Cd8a, Gzmk, Lag3, Nkg7), Cd4_Treg (Cd4, Foxp3, Tnfrsf9, Ctla4), and cycling T (Pclaf, Mki67, Stmn1). Circle size represents the percentage of expressed cells in the subtypes, and color indicates the normalized expression. (C) Proportion of T cell subtypes in each experimental groups. (D) Differential expression of inhibitory receptors (Lag3 and Tigit) in Cd8_Tem among the different experimental groups. The exhausted CD8+T cell markers, Lag3 and Tigit were significantly downregulated in the MnBuOE/RT (MnBuOE and irradiation) group compared to the RT (irradiation only) group. **P*<0.05, ***P*<0.01, ****P*<0.001. (E) Violin plot showing the expression of genes related to cytotoxicity (Gzma, Prf1), dysfunction (Pdcd1, Lag3, Tigit, Havcr2, Ctla4), and naïve/memory (Tcf, Ccr7, Il7r) scores in Cd8_Tem among the different experimental groups. **P*<0.05, ***P*<0.01, *****P*<0.0001. (F) Significant inhibitory receptor-ligand pairs (Tigit and Nectin/Pvr) or stimulatory receptor-ligand pairs (Cd226 and Nectin/Pvr) sending signals from CAFs and epithelial cells to Cd8_TemCircle size represents the levels of significance, and color shows the probability of communica. tion in each pair. MnBuOE, MnTnBuOE-2-PyP^{5+}; UMAP, uniform manifold approximation and projection; NK, natural killer; Cd8_Tem, CD8+ effector memory T cells; Cd4_Treg, CD4+ regulatory T cells; Lag3, lymphocyte-activation gene 3; Tigit, T cell immunoglobulin and immunoreceptor tyrosine-based inhibitory motif domain; MnBuOE/RT, MnTnBuOE-2-PyP^{5+}/radiation therapy; Pvr, poliovirus receptor.

3.4. T Cells Clustering and Subtype Analysis of the 4T1 Tumor Treated with MnBuOE Coupled with Irradiation

The 3,013 T cells were re-clustered into five clusters designated as natural killer (NK) T cells, naive T cells, CD8+ effector memory T cells (Cd8_Tem), CD4+ regulatory T cells (Cd4_Treg), and cycling T cells by UMAP plotting (Figure 3A). As shown in Figure 3B and Supplementary Figure S4, the functional description in the T cell compartment was determined by specific gene expression of each cluster; NK (Gzma, Tyrobp, Fcer1g), T naïve (Tcf7, Ccr7), Cd8_Tem (Cd3d, Cd3e, Cd8a, Gzmk,

 doi:10.20944/preprints202402.0355.v1

Lag3, Nkg7), Cd4_Treg (Cd4, Foxp3, Tnfrsf9, Ctla4), and Cycling T (Pclaf, Mki67, Stmn1). Subsequently, we analyzed the distribution patterns of T cell clusters among all groups (Figure 3C). Based on the distribution of T naïve and cycling T cells, the proportion of the total T cell population indicated that the lowest manifestation occurred in the MnBuOE/RT group. However, the ratio of Cd8_Tem was increased in the MnBuOE/RT group compared to the other groups. The ratio of Cd4_Treg was decreased in the MnBuOE/RT group compared to the RT group. When assessing tumor-infiltrating exhausted CD8+ T cells with exhaustion-unique gene markers such as Lag3, Tigit, Havcr2, Ctla4, and Pdcd1, we observed that the Lag3 and Tigit levels in the MnBuOE/RT group were significantly lower than those in the other groups (P<0.05, Figure 3D). T cell dysfunction scores were significantly lower in the MnBuOE/RT group than in the other groups, consistent with our data on lower levels of Treg cells and exhausted CD8+ T cells (P<0.01, Figure 3E). These results provided evidence for the differential distribution of T cell clusters, indicating an improvement in the TME of the MnBuOE/RT group. Considering the effect of Cd8_Tem in distinguishing the TME between the RT and MnBuOE/RT groups, we investigated receptor-ligand interactions across fibroblastic CAFs or epithelial cell clusters, including Cd8_Tem. The heatmap plot function was used to analyze the specific receptor-ligand interactions (rows) between two different cell types (columns) (Figure 3F). Inhibitory receptor-ligand pairs, such as T cell immunoglobulin and immunoreceptor tyrosine-based inhibitory motif domain (Tigit)-poliovirus receptor (Pvr), Tigit-Nectin2 and Tigit-Nectin3 between Cd8_Tem, and three clusters of fibroblastic CAFs, were rarely observed in the MnBuOE/RT group compared to the RT group (P<0.01). Similarly, Tigit binding affinities for Pvr and Nectin2 between Cd8_Tem and epithelial cell clusters (Epcam-, Epcam+, and cycling) were lower in the MnBuOE/RT group than in the RT group (P<0.01). Furthermore, costimulatory interactions between Cd8_Tem and epithelial cell clusters were significantly increased in the MnBuOE/RT group compared to the RT group (P<0.01), from which specific receptor-ligand complexes, Cd226-Pvr and Cd226-Nectin2, were identified. Our results suggest that MnBuOE treatment combined with irradiation in tumors can reduce Tigit-mediated inhibition of CD8+T cells while increasing Cd226-mediated T cell stimulation. Additionally, we conducted a flow cytometry of T cells in the experimental groups. The total T cell population and CD8 effective T cells were significantly increased in the MnBuOE/RT group than in the CN group and the RT group (P<0.05, Figure 4A). While Foxp3+ regulatory T cells (Tregs) tended to decrease in the MnBuOE/RT group compared to the other groups, the ratio of CD8 T cells to Tregs increased in the MnBuOE/RT group compared to the rest of the groups (P<0.05, Figure 4B).

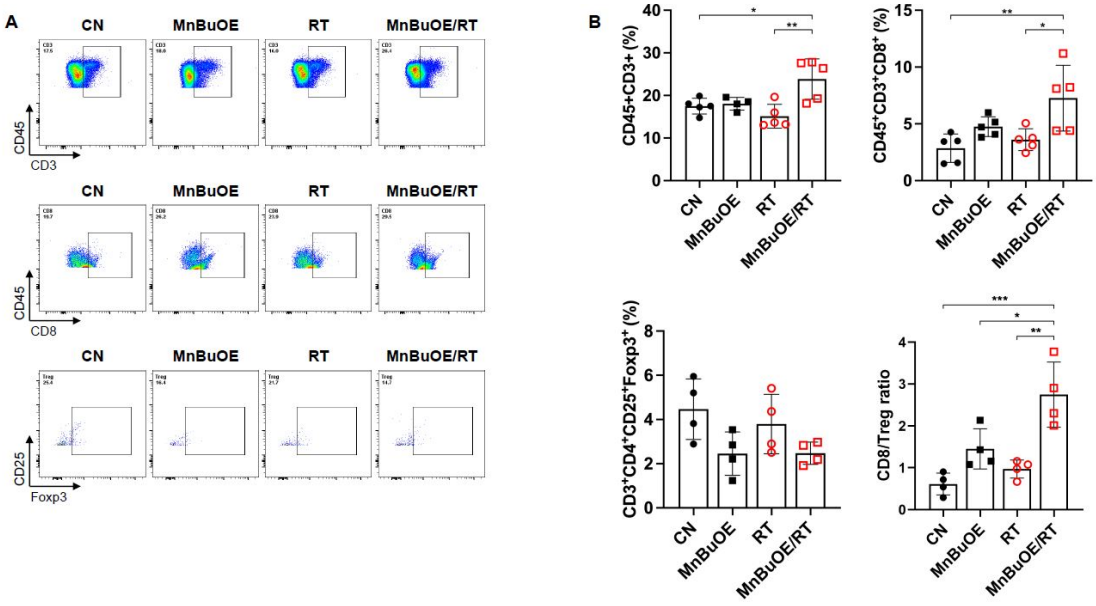

Figure 4. Flow cytometric analysis of the effects of MnBuOE and irradiation on T cell populations. **(A)** Flow cytometric analysis of total T cell population, CD8+T cells, and Treg cells infiltrated into tumors in each experimental group. Representative density plots are shown. **(B)** The proportion of

 doi:10.20944/preprints202402.0355.v1

the total T cell population, CD8+T cells, and Treg cells was calculated. These results imply that the combination of MnBuOE and irradiation can lead to increased CD8+T cells and decreased Treg cells while raising total T cell population. *P<0.05, **P<0.01, ***P<0.001. MnBuOE, MnTnBuOE-2-PyP^{5+}; Treg cells, regulatory T cells.

3.5. DC Clustering and Pseudotime Trajectory Analysis of the 4T1 Tumor Treated with MnBuOE Coupled with Irradiation

To investigate the differentiation trajectory of DC clusters, the monocle package of R software was used for the trajectory analysis. We detected four sorted DC subtypes: dendritic cell_Cd40+ (DC_Cd40+), conventional dendritic cell 1_Cd103+ (cDC1_Cd103+), conventional dendritic cell 2_Cd11b+ (cDC2_Cd11b+), and plasmacytoid dendritic cell_Siglech+ (pDC_Siglech+) (Figure 5A and Supplementary Figure S5A-B). As shown in Figure 5B, most cells from each cluster were collected based on gene signatures and the three clusters were formed via a relative process in pseudotime. The process started with the first cluster, cDC1, as they exhibited the highest level of Cd103, followed by the second cluster, cDC2, with the highest level of Cd11b, and ended with the third cluster, DC_Cd40+. The cluster of pDC equivalent to SiglecH was excluded due to its low abundance. The violin plots showed that the DC_Cd40+ cluster had high levels of various surface protein markers such as Cd40 and Cd86, which are important for DC maturation and T cell co-stimulation, and chemokine receptor Ccr7, which is involved in the migration of DCs to lymph nodes (Figure 5C). Moreover, we observed that the proportion of the DC_Cd40+ cluster increased twofold in the MnBuOE/RT group compared to the other groups, which is consistent with the high expression of Cd40, Cd80, Cd86, and Ccr7 in the MnBuOE/RT group (Figure 5D, 5E). These results indicated that MnBuOE treatment combined with irradiation facilitates DC maturation under tumor circumstances.

Preprints.org (www.preprints.org) | NOT PEER-REVIEWED | Posted: 6 February 2024 doi:10.20944/preprints202402.0355.v1

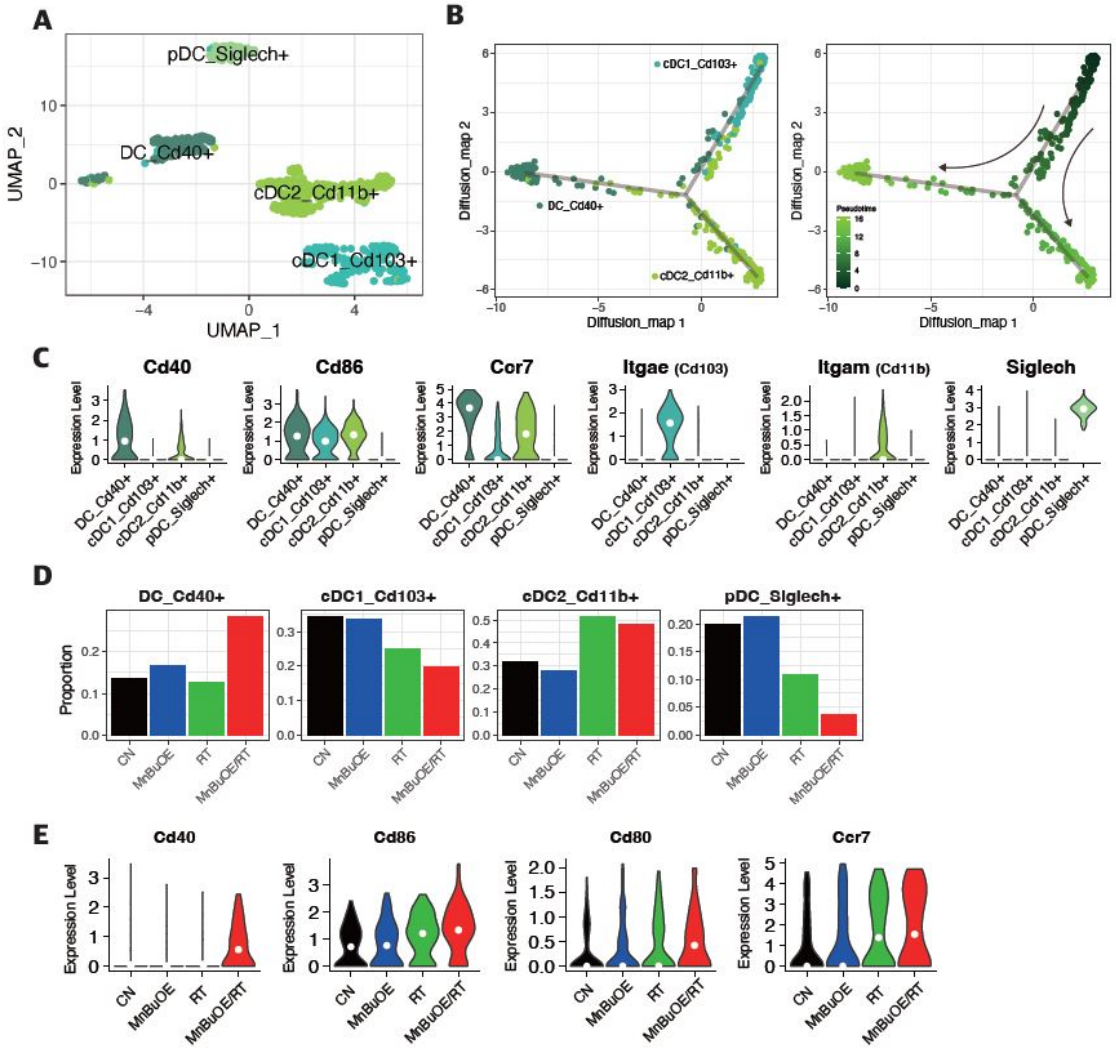

Figure 5. Effect of MnBuOE and irradiation on dendritic cell activation. (A) UMAP plot of DCs. DCs clustered in four subsets: DC_Cd40+, cDC1_Cd103+, cDC2_Cd11b+, and pDC_Siglech+. **(B)** Inferred trajectory plot using Monocle2, which shows the color-coded subtypes of DC (left) and their corresponding pseudotime (right). **(C)** Violin plot showing the expression of canonical markers in each DC subtype. The cDC2_Cd11b+ dominated Itgam, the cDC1_Cd103+ dominated Itgae, the DC_Cd40+ dominated Cd86, Cd40, Ccr7, and the pDC_Siglech+ dominated Siglech. **(D)** Proportion of DC subtypes in each experimental group. **(E)** Differential expression of co-stimulator genes (Cd40, Cd80, and Cd86) and DC markers (Ccr7) among the different experimental groups. Mature DCs were identified based on the expression of marker genes such as Cd40, Cd80, Cd86, and Ccr7. MnBuOE combined with radiation therapy triggered mature DC activation compared to the other groups. MnBuOE, MnTnBuOE-2-PyP^{5+}; UMAP, uniform manifold approximation and projection; DCs, dendritic cells; cDC, conventional dendritic cell; pDC, plasmacytoid dendritic cell.

3.6. Macrophage Clustering and Phenotype Analysis of the 4T1 Tumor Treated with MnBuOE Coupled with Irradiation

The 14,177 macrophages were clustered in seven separate subsets (Figure 6A). One cluster corresponded to myeloid-derived suppressor cells (MDSCs) (Ly6C+, Itgam+, Cxcl3+, Il1a+, Il1b+), two corresponded to M0-like macrophages (MHC II+ type and Cx3cr1+ type), one corresponded to M1-like tumor-associated macrophage (TAM) (IL1b+, Cxcl3+, Il1a+, Mmp12+), two corresponded to M2-like TAMs (Arg1+ TAM1 type and Cd206+IL10+ TAM2 type), and the final cluster corresponded to cycling macrophages (Pclaf+, Tubb5+) (Figure 6B and Supplementary Figure S6). Based on the distinction in gene signature scores between M1-like TAM, M2-like TAM, and MDSC subgroups, we

 doi:10.20944/preprints202402.0355.v1

examined the TAM polarization and estimated the change in the antitumor inflammatory reactions for all experimental groups. We observed a significant increase in the M1/M2 macrophage phenotype ratio and a significant decrease in the MDSC subgroup in the MnBuOE/RT group compared to the other groups (Figure 6C, 6D). The flow cytometry results of CD86/206 for macrophage phenotype in the experimental groups also showed that the ratio of M1/M2 phenotype increased in the MnBuOE/RT group compared to the other groups (P<0.05, Figure 6E-F). Moreover, macrophages in the MnBuOE/RT group showed significantly higher expression of inflammatory cytokines (IL-1a, IL-1b) and C-C motif chemokine ligands 3/4 (Ccl3, Ccl4) in M1-phenotype macrophages than those in the RT group (P<0.0001, Figure 6G). These results suggest that MnBuOE treatment combined with irradiation can lead to decreased MDSCs accompanied by M1 macrophage bias, which results in an anti-tumorigenic TME in tumors.

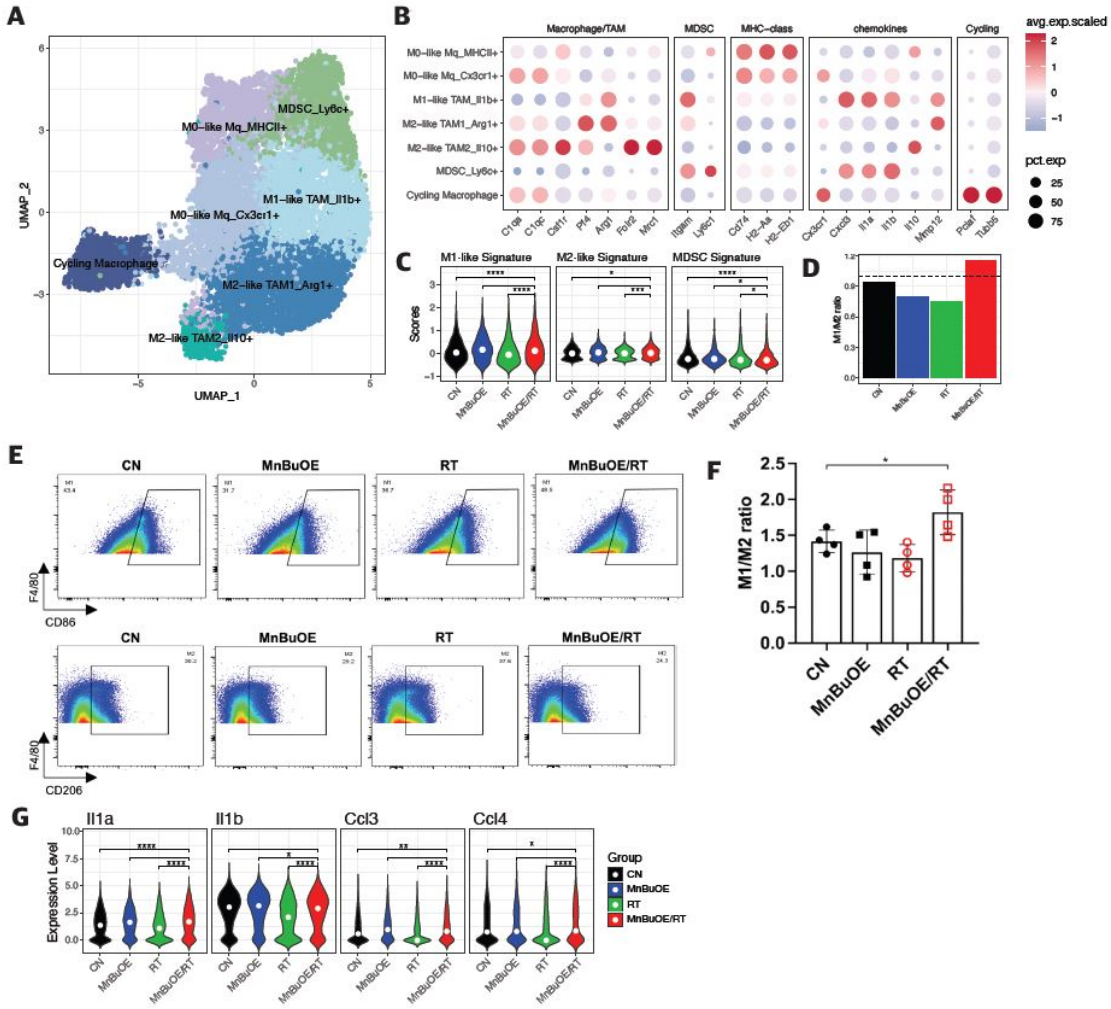

Figure 6. Increased pro-inflammatory macrophage proportion (M1-phenotype) in response to MnBuOE treatment coupled with irradiation. (A) Macrophage subtypes based on UMAP analysis presented using individual colors (n=14,177). (B) Dot plot of macrophage markers for each subtype. Two clusters correspond to M0-like macrophages (MHC II+ type and Cx3cr1+ type), one cluster corresponds to M1-like TAMs (IL1b+, Cxcl3+, Il1a+, Mmp12+), two to M2-like TAMs (Arg1+ TAM1 type and Cd206+IL10+ TAM2 type), one to MDSCs (Ly6C+, Itgam+, Cxcl3+, Il1a+, Il1b+), and the last one to cycling macrophages (Pclaf+, Tubb5+). (C) Violin plot displaying the difference in M1, M2, and MDSC scores between the experimental groups. *P<0.05, ***P<0.001, ****P<0.0001. (D) Ratio of M1-related macrophages (M1-like TAM_Il1b+) and M2-related macrophages (M2-like TAM1_Arg1+, M2-like TAM2_Il10+) in each experimental group. MnBuOE combined with irradiation therapy significantly augmented M1/M2 ratio of macrophages and reduced MDSCs compared to the other groups. (E,F) The flow cytometric analysis of M1 or M2-biased phenotype marker (CD86, CD206, or

 doi:10.20944/preprints202402.0355.v1

F4/80) for macrophage phenotype infiltrated into tumors in each experimental group. Representative density plots are shown. The ratio of M1/M2 phenotype increased in the MnBuOE/RT group compared to the other groups. *P<0.05. (G) Differential expression of inflammatory-related genes (Il1a, Il1b) and M1-phenotype genes (Ccl3, Ccl4) among the different experimental groups. *P<0.05, **P<0.01, ****P<0.0001. MnBuOE, MnTnBuOE-2-PyP^{5+}; UMAP, uniform manifold approximation and projection; TAM, tumor-associated macrophage; MDSC, myeloid-derived suppressor cells.

3.7. Intercellular Communications within TME Regulated by MnBuOE Coupled with Irradiation in the 4T1 Tumor Mice Model

To investigate potential interactions across different cell types in the TME, cell-to-cell communication analysis was performed using the CellChat database, a publicly available repository of curated receptors and ligands and their interactions. As shown in Figure 7A, the heatmap plot illustrated potential interplay with combinations across all cell subtypes between MnBuOE/RT and RT groups. The color of each square indicated relative values, based on the absolute count calculated for the intercellular interaction score of MnBuOE/RT group minus the RT group. The results showed that the number of interactions from epithelial cells, DCs, and macrophages to T cells was increased in the MnBuOE/RT group compared to the RT group. The interaction within the TME (from fibroblasts to endothelial cells) was decreased in the MnBuOE/RT group compared to the RT group. Subsequently, we investigated the number of inferred interactions, including cell–cell contact, ECM–receptor, and secreted signaling, for all experimental groups (Figure 7B). The extent of interaction for each intercellular link was lowest in the MnBuOE/RT group. These results imply that MnBuOE treatment combined with irradiation may lead to T cell communication toward DC maturation, EMT suppression, and M1 phenotypic polarization in the TME, followed by suppression of the formation of CAFs and tumor endothelial cells.

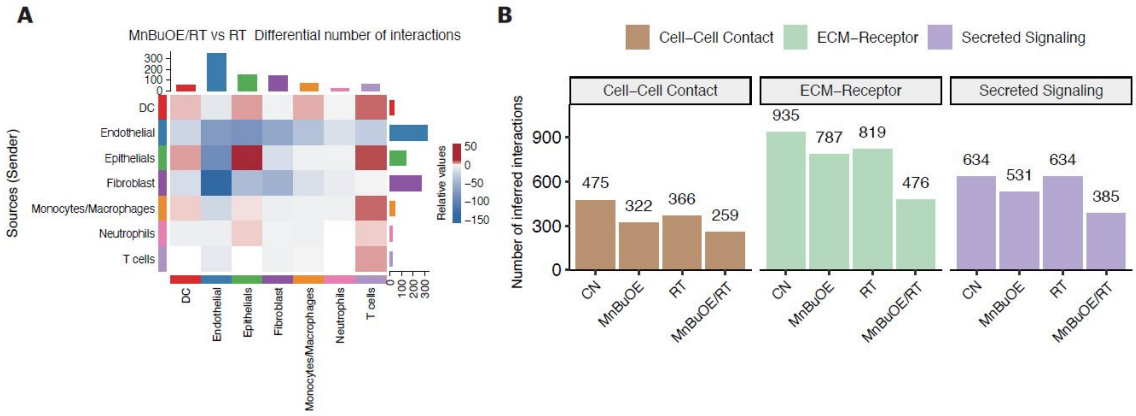

Figure 7. Difference in cell–cell interactions of TME following treatment with MnBuOE and irradiation. (A) Heatmaps showing the differential number of interactions between MnBuOE/RT (MnBuOE and irradiation) and RT (irradiation only) groups. Red color indicates increased communication in the MnBuOE/RT group compared to the RT group, whereas blue color indicates decreased possible communication. **(B)** Number of significant inferred interactions in three categories: cell–cell contact, ECM–receptor, and secreted signaling in different experimental groups. TME, tumor microenvironment; MnBuOE/RT, MnTnBuOE-2-PyP^{5+}/radiation therapy; ECM, extracellular matrix.

4. Discussion

RT remains the standard-of-care for cancer therapy; however, radiation-induced damage to normal tissues limits its effectiveness in tumor therapy. Here, we report for the first time a comprehensive characterization of the TME following Mn porphyrin clinical candidate, MnBuOE (BMX-001) treatment combined with irradiation using scRNA-seq, focusing on the various multifaceted tumor subpopulations. Progress in scRNA-seq technology has enabled the compositional analysis of the immune system at single-cell levels and permitted the identification

 doi:10.20944/preprints202402.0355.v1

and sub-clustering of major cell subsets of the TME, exploration of cell type-, molecular pathway- and etiology-specific gene signatures, and prediction of putative cell–cell interactions [32]. Our analysis identified eight distinct cell populations with UMAP clustering of tumor tissues. Those were mapped into 4 non-immune types of epithelial cells, fibroblasts, endothelial cells, and myocytes and 4 immune clusters of macrophages, neutrophils, T cells, and DCs.

Among the epithelial cell subtypes, the unique functions of Epi1_Epcam- cells and Epi2_Epcam+ cells were strongly associated with EMT, which can invade surrounding tissues and travel through the peripheral circulation. The distribution of these epithelial subtypes enables the understanding of the metastasis hypothesis in epithelial cells. The GSEA of epithelial cells confirms that enrichment pathway scores associated with EMT, TNF-alpha signaling via NF-kB, angiogenesis, and hypoxia were significantly decreased in the MnBuOE/RT group compared to the RT group, which is consistent with our previous report [18]. Furthermore, we divided fibroblasts into myofibroblastic, inflammatory, and cycling CAFs. CAFs have been reported as a key component of the TME [24], and are a strong source of chemokine CXCL12 and rich in alpha-smooth muscle actin-positive cells, which promote tumor growth and angiogenesis and remodel the ECM [33–35]. Additionally, CAFs inhibit the function of CD8+ T cells, promote Treg recruitment, and suppress their tumor cell-killing abilities by reducing T cell infiltration into the tumor, thus impeding T cell trafficking within the TME and inhibiting cytotoxic activity [36]. In this study, we observed that treatment with MnBuOE reduces CAFs, which may substantially contribute to preventing cancer metastasis.

Subsequently, we investigated five major T cell clusters, including NKT, T naive, CD8+ effector memory T cells, CD4+ Tregs, and the remaining T cells to reveal the intrinsic structure and potential functional subtypes of the overall T cell populations. T cells within the TME are prone to either dysfunction or exhaustion, thus preventing CD8+ T cells from eliciting sufficient T cell-mediated killing of tumor cells [22,37]. Our data demonstrate that the proportion of CD8+ effector memory T cells increased, whereas CD4+ Tregs decreased when mice were treated with MnBuOE/RT compared to treatment with RT alone. CD8+ T cells, in particular, are important targets in cancer immunotherapy, making them the focus of numerous single-cell studies. Building on these studies, we recapitulated the heterogeneity of CD8+ T cells according to cytotoxic, dysfunctional, and naïve-like cell states. The expression of CD8+ T cell exhaustion markers, such as Lag3 and Tigit, was significantly lower in the MnBuOE/RT group than in the RT group, leading to alleviation of T cell dysfunction and restoration of T cell infiltration.

Additionally, intimate cell–cell communications across CAFs or epithelial cell clusters, including CD8+ T cells, were analyzed within the TME. We observed a significant decrease in coinhibitory interactions, such as those among Tigit-Pvr, Tigit-Nectin2, and Tigit-Nectin3, in the MnBuOE/RT group compared to the RT group, whereas a significant increase in costimulatory interactions, such as those between CD226-Pvr and CD226-Nectin2, was observed in the MnBuOE/RT group compared to the RT group. The correlation of high Tigit expression with a poor clinical outcome is consistent with the view that one of the functions of Tigit is the formation of an immunosuppressive TME [38–40]. While Tigit functions as an inhibitory receptor, CD226 has been known to play important roles in T cell priming and activation. Focusing on the CD8+ T cells in these studies, MnBuOE treatment combined with irradiation may control the Tigit/CD226 imbalance by suppressing exhausted CD8+ T cells within the TME.

DCs are essential for T cell-mediated cancer immunity [41]. In particular, the distinguishing directivity of cDCs to stimulate T cells leads to the maturation of DCs and the expression of CD40, CD80, and CD86. We identified the differentiation trajectory of three clusters of DCs, which were formed via a relative process in pseudotime. The differentiation trajectory begins with the CD103+ dominant cDC1 subtype and proceeds with the CD11B+ dominant cDC2 cluster and CD40+ dominant mature DC cluster. We observed a significant increase in the proportion of CD40+ dominant mature DCs in the MnBuOE/RT group compared to that in the other groups. Our results, along with those of previous reports, suggest that MnBuOE/RT treatment efficacy leads to DC maturation and co-stimulation between DCs and CD8+ T cells, thereby resulting in tumor regression.

 doi:10.20944/preprints202402.0355.v1

Accumulating evidence suggests that TAMs are a heterogeneous group of cells with multiple mechanisms involved in promoting tumor progression [42–44]. MDSCs are another heterogeneous population of cells that expand during cancer progression, which can also suppress T-cell responses. In our scRNA-seq analysis data, macrophages were largely separated into unpolarized M0-like macrophages and polarized M1 and M2 macrophages, including MDSCs. Studies indicate that the M1-like macrophages are pro-inflammatory and release various cytotoxic molecules that are crucial to suppressing tumorigenesis. Conversely, the predominance of M2-like macrophages causes tumor progression. We observed a clear increase in the M1/M2 ratio and a significant decrease in MDSCs in the MnBuOE/RT group compared to the other groups. We further confirmed that both inflammatory cytokines, IL-1a and IL-1b, and chemokines CCL3 and CCL4 inducing M1-polarization, which were reduced by irradiation, were significantly increased following the MnBuOE/RT treatment. Our results, along with those of previous reports [10], suggest that MnBuOE/RT can reduce levels of M2-polarized macrophages while inhibiting MDSCs induced by irradiation of tissues.

Analysis of cell–cell interactions based on the expression of ligand-receptor pairs in different cell types can aid in understanding how intimately major cell types interact. Our results showed that the number of T-cell trafficking of DCs, macrophages, and epithelial cells was higher in the MnBuOE/RT group than in the RT group, whereas the number of T-cell exchanges of fibroblasts and endothelial cells was low. In particular, the MnBuOE/RT group had fewer affected ECM receptors or activated intracellular signaling pathways than the other groups. Thus, our data have demonstrated that treatment of cancer using a combination of MnBuOE and RT could increase CD8+T cytotoxicity through DC maturation and inflammatory-like macrophages and directly kill tumor cells by lowering the interaction of exhausted CD8+ T cells with epithelial cells and fibroblasts. It could also decrease levels of CAFs and prevent epithelial cells from progressing to EMT, angiogenesis, and inflammation, resulting in protection against the damage to the surrounding normal cells (Figure 8). However, we could not exclude the possibility that MnBuOE/RT can differentially regulate the inflammatory process according to cell types in the TME. Therefore, differential oxidative stress of certain cells may play a role in the underlying mechanism of action of Mn porphyrin in promoting tumor growth suppression and normal tissue protection. Taken together, our data provide another perspective on the anticancer effect of MnBuOE/RT using the database of genes related to the signaling pathways of each cell type within the TME.

 doi:10.20944/preprints202402.0355.v1

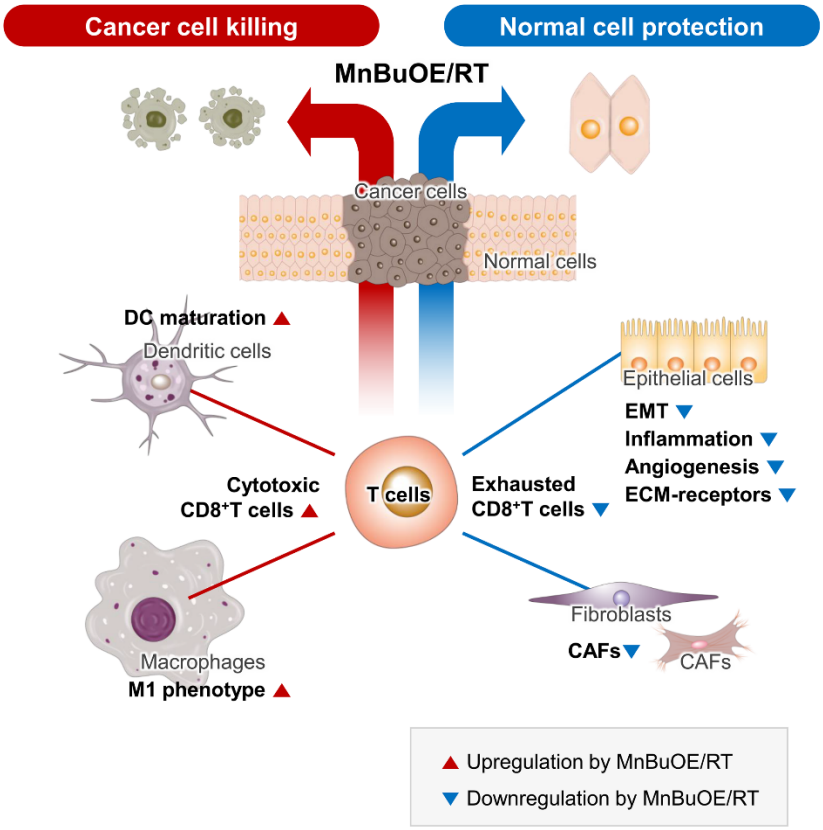

Figure 8. Schematic diagram of the synergistic effect of MnBuOE/RT in cancer treatment. By analyzing the characteristics of each subtype formed by tumor and immune cells in the TME, we discussed the possibility that each cell would interact organically with other cells with cell specificity. Our data suggest that MnBuOE/RT therapy can provide a favorable environment for cancer cell removal due to M1-macrophage, DC maturation, and augmented cytotoxic CD8+T activity, which in turn prevents normal cell damage and metastasis, induced by inflammation and angiogenesis by inhibiting CAFs and EMT. MnBuOE/RT, MnTnBuOE-2-PyP^{5+}/radiation therapy; TME, tumor microenvironment; DC, dendritic cell; CAFs, cancer-associated fibroblasts; EMT, epithelial-to-mesenchymal transition.

5. Conclusions

Mn porphyrins, commonly known as SOD mimic, have been reported to increase radiation treatment efficiency by protecting normal tissues while having radiosensitivity of tumors, and has shown effective clinical results in various cancers. However, it is necessary to find how Mn porphyrins work in response to the heterogeneity of various cells in the tumor microenvironment. We for the first time explored the mechanisms underlying immunomodulation of a novel Mn porphyrin clinical candidate, MnTnBuOE-2-PyP^{5+} (BMX-001), using single-cell analysis in murine mammary carcinoma model. We demonstrated that MnTnBuOE-2-PyP^{5+} and irradiation could kill tumor cells and prevent metastasis by increasing CD8+ T cells through dendritic cell activation and increasing M1 macrophages while reducing cancer-associated fibroblasts and inhibiting angiogenesis and inflammatory responses of epithelial cells. This study reveals the anticancer synergistic effect of BMX-001/radiotherapy at a single-cell level for various cells that comprise tumor heterogeneity, and presented another perspective on the changes in the tumor microenvironment.

Supplementary Materials: The following supporting information can be downloaded at the website of this paper posted on Preprints.org, Figure S1: Quality-control of scRNA-seq and annotation of major clusters; Figure S2: Identification of epithelial cell clusters; Figure S3: Decreased number of fibroblasts following treatment with

MnBuOE and irradiation; Figure S4: Characterizing of T and NK cell clusters; Figure S5: Identification of dendritic cell clusters; Figure S6: Characterization of seven myeloid cell subsets.

Author Contributions: Conceptualization, S.U.N., C.C., and W.P.; Investigation, S.U.N., C.C., and W.P.; Methodology, S.U.N., J.L., S.-W.S. and Y.K.; Formal Analysis, S.U.N., J.L. and C.C.; Resources, I.B.-H. and W.-Y.P.; Visualization, S.U.N., J.L., and Y.K.; Writing - Original Draft, S.U.N. and J.L.; Writing -Review and Editing, S.U.N., I.B.-H., C.C. and W.P.; Project Administration, C.C. and W.P.; Supervision, W.P.; Funding Acquisition, W.P. All authors have read and agreed to the published version of the manuscript.

Funding: This work was supported by the National Research Foundation of Korea (NRF) grant funded by the Korean government (MSIT) (NRF-2019R1A2C2002304, NRF-2023R1A2C2003774).

Institutional Review Board Statement: The study protocol (20220210001) was reviewed and approved by the Institutional Animal Care and Use Committee (IACUC) of the Samsung Medical Center (SMC). SMC is an Association for Assessment and Accreditation of Laboratory Animal Care International accredited facility and abides by the Institute of Laboratory Animal Resources guidelines.

Informed Consent Statement: Not applicable.

Date Availability Statement: Data is contained within the article or Supplementary Material.

Conflicts of Interest: I.B.-H. and Duke University have patent rights and licensed technologies to BioMimetix JVLLC. I.B.-H. holds equities and is consultant for BioMimetix JVLLC. None of the conflicts affected the experimental design, interpretation, and reporting of the results. The other authors declare no competing interest.

References

1. D.G. Franchina; C. Dostert; D. Brenner. Reactive Oxygen Species: Involvement in T Cell Signaling and Metabolism. Trends Immunol. **2018**, *39*, 489-502.
2. X. Chen; M. Song; B. Zhang; Y. Zhang. Reactive Oxygen Species Regulate T Cell Immune Response in the Tumor Microenvironment. Oxid Med Cell Longev. **2016**, *2016*, 1580967.
3. E.L. Yarosz; C.H. Chang. The Role of Reactive Oxygen Species in Regulating T Cell-mediated Immunity and Disease. Immune Netw. **2018**, *18*, e14.
4. S.Y. Lee; E.K. Jeong; M.K. Ju; H.M. Jeon; M.Y. Kim; C.H. Kim; H.G. Park; S.I. Han; H.S. Kang. Induction of metastasis, cancer stem cell phenotype, and oncogenic metabolism in cancer cells by ionizing radiation. Molecular Cancer **2017**, *16*, 10.
5. I. Batinic-Haberle; A. Tovmasyan; Z. Huang; W. Duan; L. Du; S. Siamakpour-Reihani; Z. Cao; H. Sheng; I. Spasojevic; A. Alvarez Secord. H(2)O(2)-Driven Anticancer Activity of Mn Porphyrins and the Underlying Molecular Pathways. Oxid Med Cell Longev. **2021**, *2021*, 6653790.
6. I. Batinic-Haberle; A. Tovmasyan; I. Spasojevic. Mn Porphyrin-Based Redox-Active Drugs: Differential Effects as Cancer Therapeutics and Protectors of Normal Tissue Against Oxidative Injury. Antioxid Redox Signal. **2018**, *29*, 1691-1724.
7. I. Batinic-Haberle; M.E. Tome. Thiol regulation by Mn porphyrins, commonly known as SOD mimics. Redox Biol. **2019**, *25*, 101139.
8. S.R. Birer; C.T. Lee; K.R. Choudhury; K.H. Young; I. Spasojevic; I. Batinic-Haberle; J.D. Crapo; M.W. Dewhirst; K.A. Ashcraft. Inhibition of the Continuum of Radiation-Induced Normal Tissue Injury by a Redox-Active Mn Porphyrin. Radiat Res. **2017**, *188*, 94-104.
9. Y. Yulyana; A. Tovmasyan; I.A. Ho; K.C. Sia; J.P. Newman; W.H. Ng; C.M. Guo; K.M. Hui; I. Batinic-Haberle; P.Y. Lam. Redox-Active Mn Porphyrin-based Potent SOD Mimic, MnTnBuOE-2-PyP(5+), Enhances Carbenoxolone-Mediated TRAIL-Induced Apoptosis in Glioblastoma Multiforme. Stem Cell Rev Rep. **2016**, *12*, 140-55.
10. K.A. Ashcraft; M.K. Boss; A. Tovmasyan; K. Roy Choudhury; A.N. Fontanella; K.H. Young; G.M. Palmer; S.R. Birer; C.D. Landon; W. Park; S.K. Das; T. Weitner; H. Sheng; D.S. Warner; D.M. Brizel; I. Spasojevic; I. Batinic-Haberle; M.W. Dewhirst. Novel Manganese-Porphyrin Superoxide Dismutase-Mimetic Widens the Therapeutic Margin in a Preclinical Head and Neck Cancer Model. Int J Radiat Oncol Biol Phys. **2015**, *93*, 892-900.
11. A. Flórido; N. Saraiva; S. Cerqueira; N. Almeida; M. Parsons; I. Batinic-Haberle; J.P. Miranda; J.G. Costa; G. Carrara; M. Castro; N.G. Oliveira; A.S. Fernandes. The manganese(III) porphyrin MnTnHex-2-PyP(5+) modulates intracellular ROS and breast cancer cell migration: Impact on doxorubicin-treated cells. Redox Biol. **2019**, *20*, 367-378.
12. M.K. Boss; R.E. Oberley-Deegan; I. Batinic-Haberle; G.A. Talmon; J.A. Somarelli; S. Xu; E.A. Kosmacek; B. Griess; S. Mir; S. Shrishrimal; M. Teoh-Fitzgerald; I. Spasojevic; M.W. Dewhirst. Manganese Porphyrin and

Radiotherapy Improves Local Tumor Response and Overall Survival in Orthotopic Murine Mammary Carcinoma Models. Radiat Res. **2021**, *195*, 128-139.

13. A. Chatterjee; Y. Zhu; Q. Tong; E.A. Kosmacek; E.Z. Lichter; R.E. Oberley-Deegan. The Addition of Manganese Porphyrins during Radiation Inhibits Prostate Cancer Growth and Simultaneously Protects Normal Prostate Tissue from Radiation Damage. Antioxidants (Basel) **2018**, *7*, 21.
14. E.A. Kosmacek; A. Chatterjee; Q. Tong; C. Lin; R.E. Oberley-Deegan. MnTnBuOE-2-PyP protects normal colorectal fibroblasts from radiation damage and simultaneously enhances radio/chemotherapeutic killing of colorectal cancer cells. Oncotarget **2016**, *7*, 34532-45.
15. Z. Rajic; A. Tovmasyan; O.L. de Santana; I.N. Peixoto; I. Spasojevic; S.A. do Monte; E. Ventura; J.S. Rebouças; I. Batinic-Haberle. Challenges encountered during development of Mn porphyrin-based, potent redox-active drug and superoxide dismutase mimic, MnTnBuOE-2-PyP(5+), and its alkoxyalkyl analogues. J Inorg Biochem. **2017**, *169*, 50-60.
16. Katherine Peters; Adam Cohen; Nicholas Butowski; John Villano; Joe Mendez; Pierre Giglio; Tresa McGranahan; Chi Zhang; Jacob Smeltzer; Shahzad Raza; Burt Nabors; Mina Lobbous; James Herndon; Evan Buckley; David MacLeod; Sara Penchev; David Silberstein; Ines Batinic-Haberle; Ivan Spasojevic; Shayne Gad; David Radoff; Daniel Barboriak; James Crapo. LTBK-09. RESULTS OF BMX-HGG STUDY: A MULTI-INSTITUTIONAL, RANDOMIZED PHASE 2 CLINICAL TRIAL OF CONCURRENT CHEMORADIATION WITH OR WITHOUT BMX-001 IN PATIENTS WITH NEWLY DIAGNOSED HIGH GRADE GLIOMA. Neuro-oncology **2023**, doi:10.1093/neuonc/noad179.1203.
17. S.W. Shin; C. Choi; G.H. Lee; A. Son; S.H. Kim; H.C. Park; I. Batinic-Haberle; W. Park. Mechanism of the Antitumor and Radiosensitizing Effects of a Manganese Porphyrin, MnHex-2-PyP. Antioxid Redox Signal. **2017**, *27*, 1067-1082.
18. S.W. Shin; C. Choi; H. Kim; Y. Kim; S. Park; S.Y. Kim; I. Batinic-Haberle; W. Park. MnTnHex-2-PyP(5+), Coupled to Radiation, Suppresses Metastasis of 4T1 and MDA-MB-231 Breast Cancer via AKT/Snail/EMT Pathways. Antioxidants (Basel) **2021**, *10*, 1769.
19. S. Shrishrimal; A. Chatterjee; E.A. Kosmacek; P.J. Davis; J.T. McDonald; R.E. Oberley-Deegan. Manganese porphyrin, MnTE-2-PyP, treatment protects the prostate from radiation-induced fibrosis (RIF) by activating the NRF2 signaling pathway and enhancing SOD2 and sirtuin activity. Free Radic Biol Med. **2020**, *152*, 255-270.
20. O.M. Ozpiskin; L. Zhang; J.J. Li. Immune targets in the tumor microenvironment treated by radiotherapy. Theranostics **2019**, *9*, 1215-1231.
21. E. Lo Presti; F. Dieli; S. Meraviglia. Tumor-Infiltrating γδ T Lymphocytes: Pathogenic Role, Clinical Significance, and Differential Programing in the Tumor Microenvironment. Front Immunol. **2014**, *5*, 607.
22. Y. Jiang; Y. Li; B. Zhu. T-cell exhaustion in the tumor microenvironment. Cell Death Dis**. 2015**, *6*, e1792.
23. S. Brassart-Pasco; S. Brézillon; B. Brassart; L. Ramont; J.B. Oudart; J.C. Monboisse. Tumor Microenvironment: Extracellular Matrix Alterations Influence Tumor Progression. Front Oncol. **2020**, *10*, 397.
24. M.B. Giorello; F.R. Borzone; V. Labovsky; F.V. Piccioni; N.A. Chasseing. Cancer-Associated Fibroblasts in the Breast Tumor Microenvironment. J Mammary Gland Biol Neoplasia **2021**, *26*, 135-155.
25. M.L. Suvà; I. Tirosh. Single-Cell RNA Sequencing in Cancer: Lessons Learned and Emerging Challenges. Molecular Cell **2019**, *75*, 7-12.
26. J.J. Quinn; M.G. Jones; R.A. Okimoto; S. Nanjo; M.M. Chan; N. Yosef; T.G. Bivona; J.S. Weissman. Single-cell lineages reveal the rates, routes, and drivers of metastasis in cancer xenografts. Science **2021**, *371*, eabc1944.
27. Y. Hao; S. Hao; E. Andersen-Nissen; W.M. Mauck 3rd; S. Zheng; A. Butler; M.J. Lee; A.J. Wilk; C. Darby; M. Zager; P. Hoffman; M. Stoeckius; E. Papalexi; E.P. Mimitou; J. Jain; A. Srivastava; T. Stuart; L.M. Fleming; B. Yeung; A.J. Rogers; J.M. McElrath; C.A. Blish; R. Gottardo; P. Smibert; R. Satija. Integrated analysis of multimodal single-cell data. Cell **2021**, *184*, 3573-3587.e29.
28. G. Finak; A. McDavid; M. Yajima; J. Deng; V. Gersuk; A.K. Shalek; C.K. Slichter; H.W. Miller; M.J. McElrath; M. Prlic; P.S. Linsley; R. Gottardo. MAST: a flexible statistical framework for assessing transcriptional changes and characterizing heterogeneity in single-cell RNA sequencing data. Genome Biol. **2015**, *16*, 278.
29. G. Korotkevich; V. Sukhov; N. Budin; B. Shpak; M.N. Artyomov; A. Sergushichev. Fast gene set enrichment analysis. bioRxiv. **2021**, doi:10.1101/060012.
30. X. Qiu; A. Hill; J. Packer; D. Lin; Y.A. Ma; C. Trapnell. Single-cell mRNA quantification and differential analysis with Census. Nat Methods **2017**, *14*, 309-315.
31. S. Jin; C.F. Guerrero-Juarez; L. Zhang; I. Chang; R. Ramos; C.H. Kuan; P. Myung; M.V. Plikus; Q. Nie. Inference and analysis of cell-cell communication using CellChat. Nat Commun. **2021**, *12*, 1088.
32. W. Chung; H.H. Eum; H.O. Lee; K.M. Lee; H.B. Lee; K.T. Kim; H.S. Ryu; S. Kim; J.E. Lee; Y.H. Park; Z. Kan; W. Han; W.Y. Park. Single-cell RNA-seq enables comprehensive tumour and immune cell profiling in primary breast cancer. Nat Commun. **2017**, *8*, 15081.

 doi:10.20944/preprints202402.0355.v1

33. D. Lavie; A. Ben-Shmuel; N. Erez; R. Scherz-Shouval. Cancer-associated fibroblasts in the single-cell era. Nat Cancer **2022**, *3*, 793-807.
34. F. Wu; J. Yang; J. Liu; Y. Wang; J. Mu; Q. Zeng; S. Deng; H. Zhou. Signaling pathways in cancer-associated fibroblasts and targeted therapy for cancer. Signal Transduct Target Ther. **2021**, *6*, 218.
35. J. Winkler; A. Abisoye-Ogunniyan; K.J. Metcalf; Z. Werb. Concepts of extracellular matrix remodelling in tumour progression and metastasis. Nat Commun. **2020**, *11*, 5120.
36. A.T. Baker; M.H. Abuwarwar; L. Poly; S. Wilkins; A.L. Fletcher. Cancer-Associated Fibroblasts and T Cells: From Mechanisms to Outcomes. J Immunol. **2021**, *206*, 310-320.
37. A.M. van der Leun; D.S. Thommen; T.N. Schumacher. CD8(+) T cell states in human cancer: insights from single-cell analysis. Nat Rev Cancer **2020**, *20*, 218-232.
38. K.E. Pauken; E.J. Wherry. TIGIT and CD226: tipping the balance between costimulatory and coinhibitory molecules to augment the cancer immunotherapy toolkit. Cancer Cell **2014**, *26*, 785-787.
39. E.Y. Chiang; I. Mellman. TIGIT-CD226-PVR axis: advancing immune checkpoint blockade for cancer immunotherapy. J Immunother Cancer **2022**, *10*, e004711.
40. J. Yeo; M. Ko; D.H. Lee; Y. Park; H.S. Jin. TIGIT/CD226 Axis Regulates Anti-Tumor Immunity. Pharmaceuticals (Basel) **2021**, *14*, 200.
41. A. Gardner; B. Ruffell. Dendritic Cells and Cancer Immunity. Trends Immunol. **2016**, *37*, 855-865.
42. T. Hourani; J.A. Holden; W. Li; J.C. Lenzo; S. Hadjigol; N.M. O'Brien-Simpson. Tumor Associated Macrophages: Origin, Recruitment, Phenotypic Diversity, and Targeting. Front Oncol. **2021**, *11*, 788365.
43. T.D. Ricketts; N. Prieto-Dominguez; P.S. Gowda; E. Ubil. Mechanisms of Macrophage Plasticity in the Tumor Environment: Manipulating Activation State to Improve Outcomes. Front Immunol. **2021**, *12*, 642285.
44. D.I. Gabrilovich; S. Nagaraj. Myeloid-derived suppressor cells as regulators of the immune system. Nat Rev Immunol. **2009**, *9*, 162-74.